




<https://doi.org/10.1038/s42003-024-07106-4>

# Unveiling the impact of hypodermis on gene expression for advancing bioprinted full-thickness 3D skin models



Thayná M. Avelino<sup>1</sup>, Samarah V. Harb<sup>1</sup>, Douglas Adamoski<sup>1</sup> , Larissa C. M. Oliveira<sup>1</sup>, Cintia D. S. Horinouchi<sup>1</sup>, Rafael J. de Azevedo<sup>1</sup>, Rafael A. Azoubel<sup>2</sup>, Vanessa K. Thomaz<sup>1</sup>, Fernanda A. H. Batista<sup>1,3</sup>, Marcos Akira d'Ávila<sup>2</sup>, Pedro L. Granja<sup>4,5</sup> & Ana Carolina M. Figueira<sup>1</sup>  


3D skin models have been explored as an alternative method to the use of animals in research and development. Usually, human skin equivalents comprise only epidermis or epidermis/dermis layers. Herein, we leverage 3D bioprinting technology to fabricate a full-thickness human skin equivalent with hypodermis (HSEH). The collagen hydrogel-based structure provides a mimetic environment for skin cells to adhere, proliferate and differentiate. The effective incorporation of the hypodermis layer is evidenced by scanning electron microscopy, immunofluorescence, and hematoxylin and eosin staining. The transcriptome results underscore the pivotal role of the hypodermis in orchestrating the genetic expression of a multitude of genes vital for skin functionality, including hydration, development and differentiation. Accordingly, we evidence the paramount significance of full-thickness human skin equivalents with hypodermis layer to provide an accurate in vitro platform for disease modeling and toxicology studies.

Skin tissue engineering is a field which greatly evolved in the last 5 decades. Elucidation of skin physiopathology, together with biotechnology evolution, allowed the development of an assortment of skin substitute templates which are intended for medical approaches and scientific purposes including in vitro modeling of skin disorders and testing of pharmaceutical products<sup>1</sup>. Advanced techniques and modern strategies of biofabrication led to the assembly of complex tissue engineered skin models which efficiently mimic some skin conditions, including atopic dermatitis, melanoma, and others, although none of these fully recapitulate the heterogeneity of natural skin biology and physiopathology<sup>2</sup>.

The expectation for bioengineered skin models is to recapitulate the physiology of human skin to be applied as a non-clinical human model with more predictability than animal models in the search for new therapeutic strategies, or in the elucidation of the pathophysiology of skin disorders<sup>3-5</sup>. For this purpose, they should mimic the natural biology and structure of the skin. Considering the importance of each skin layer for its integrity and functionality, an ideal model should present an equally 3-layered structure. However, most of the currently available models present only 1 or 2-layered tissues<sup>1,2,4,6-11</sup>. Although dermis and epidermis have been proved to be efficiently mimicked, hypodermis is frequently omitted<sup>1</sup>.

The diversity of the essential skin functions like immune and physical protection, thermoregulation, water content regulation, and others, is only possible because of the highly complex biology of the organ, composed by the 3 main structural layers: epidermis, dermis, and hypodermis<sup>12</sup>. Hypodermis, also known as subcutaneous layer, was functionally underestimated for a long time. Nowadays, it is well-known that the hypodermis is not just a storage of energy or a source of padding and insulation for the body. It is also profoundly involved in immune process and homeostasis, exerting a dynamic influence over the other skin layers<sup>13</sup>. The involvement and importance of the hypodermis in skin disorders such as metabolic syndrome, burns, and scarring has been increasingly put in evidence<sup>14,15</sup>.

Despite the acknowledged physiological importance of the hypodermis, its integration into full-thickness skin models has been limited. Previous studies have incorporated this layer by introducing mature human primary adipocytes or by differentiating human adipose mesenchymal stem cells into adipocytes. These models demonstrated that the presence of adipocytes supports the maturation and differentiation of epidermal cells, which is crucial for maintaining barrier functionality and integrity<sup>13,16</sup>. Recently, a 3-layered skin model showed that adipocytes presence improved dermal-epidermal junction quality and rete ridge-like structures when compared to a

<sup>1</sup>Brazilian Center for Research in Energy and Materials (CNPem), OKNational Laboratory of Bioscience (LNBio), Campinas, Brazil. <sup>2</sup>Department of Manufacturing and Materials Engineering, School of Mechanical Engineering, Universidade Estadual de Campinas (UNICAMP), Campinas, Brazil. <sup>3</sup>Molecular Research Laboratory in Cardiology, Dante Pazzanese Institute of Cardiology (IDPC), São Paulo, Brazil. <sup>4</sup>Instituto de Investigação e Inovação em Saúde (i3S), Universidade do Porto, Porto, Portugal. <sup>5</sup>Instituto Nacional de Engenharia Biomédica (INEB), Universidade do Porto, Porto, Portugal.  e-mail: [ana.figueira@lnbio.cnpem.br](mailto:ana.figueira@lnbio.cnpem.br)

bi-layered skin model<sup>5</sup>. Another study focused on the development of a 3-layered skin model to obtain a reliable in vitro platform for studying diabetic skin wound healing<sup>17</sup>. Additionally, 3-layered bioprinted skin graft has been applied for skin wound healing in different animal models<sup>8</sup>. In contrast to these approaches, our goal was to develop a simplified, cost-effective full-thickness skin model to assess the physiological relevance of in vitro systems for creating reliable humanized tissues applicable in cosmetic, pharmaceutical, and basic research. Our approach employs a straightforward fabrication process using only human primary keratinocytes, human primary fibroblasts, and adipocytes from differentiated human mesenchymal stem cells embedded in a collagen-based matrix. Through transcriptomic analysis, we unveiled the significant impact of the hypodermis on gene expression for advancing our 3D skin models. The Human Skin Equivalent with Hypodermis (HSEH) developed in this study not only faithfully replicated the architectural layers of native skin but also upregulated specific markers associated with adipose tissue, skin differentiation, and hydration, which are involved in key

biological processes. The HSEH emerged as a promising and ethically responsible tool for advancing dermatological research and reducing the need for animal experimentation.

## Results and discussion

### Collagen properties

As collagen is the major component of the extracellular matrix in the dermis and hypodermis, we conducted a thorough characterization of this material. Rheological measurements have indicated that the collagen solution behaves differently in the presence or absence of cells (Fig. 1a). In the absence of cells, the collagen solution exhibits Bingham plastic-like behavior at low shear rates, attributed to the entanglement of collagen molecules. However, once the shear rate exceeds a critical threshold, the material undergoes a transition to shear-thinning behavior. This occurs due to the alignment of protein chains in the direction of flow, which increases with rising shear rate<sup>18</sup>. In the cellular collagen solution, the cells hinder the

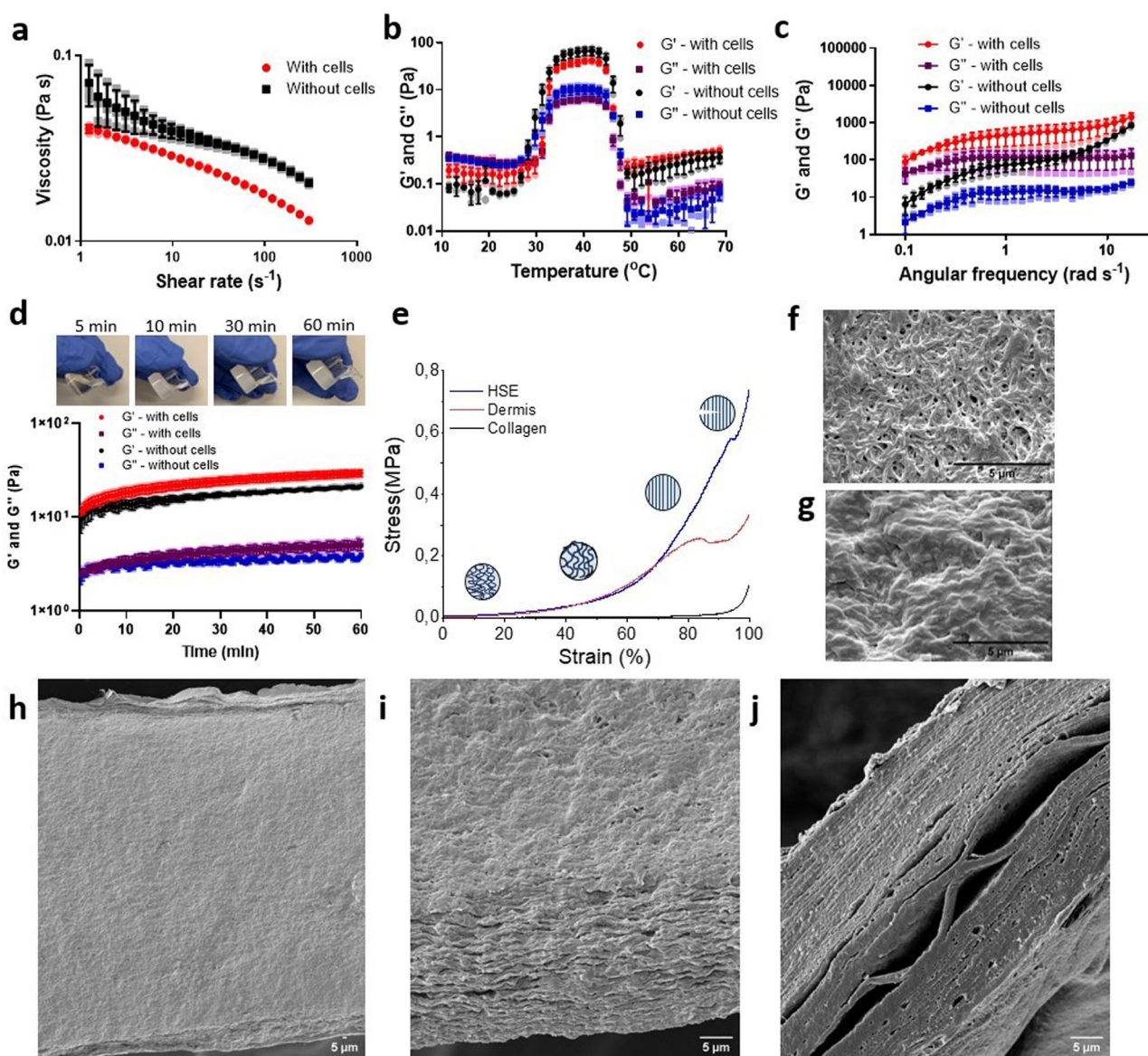


**Fig. 1 | Rheological, mechanical, and morphological properties of collagen.** a Shear rate sweep and (b) temperature sweep of non-crosslinked collagen with and without fibroblasts. c Frequency sweep of crosslinked collagen with and without fibroblasts. d Time sweep at 37 °C of collagen solutions with and without fibroblasts. e Stress-strain curves of crosslinked collagen without fibroblasts, dermis (collagen +

fibroblasts), and human skin equivalent (HSE). Scanning electron microscopy (SEM) of the crosslinked collagen (f) without and (g) with fibroblasts. Scanning electron micrographs of HSEH after 10 days of maturation. h shows the full thickness images, (i) shows the hypodermis region and (j) epidermis layer. In the graphs (a–d) error bars are resultant from  $n = 3$ .

collagen aggregation, therefore it behaves as a non-Newtonian fluid with a pseudoplastic behavior throughout the analyzed shear rate range. Pseudoplastic materials are fluids that exhibit a decrease in viscosity with an increase in the shear rate. In other words, they become less viscous when subjected to higher shear forces. This shear-thinning behavior is advantageous for bioinks because as the ink is extruded through the syringe nozzle, shear occurs and viscosity decreases, thus allowing the material to flow more easily<sup>19</sup>. This facilitates the controlled extrusion of material through the fine printing tips and the precise deposition of the desired patterns<sup>20</sup>. After deposition, the viscosity of the bioink increases, assisting in maintaining the integrity of the printed structure. In collagen, the shear-thinning is caused by the disentanglement of collagen chains during flow<sup>21</sup>. The presence of fibroblast into the collagen matrix slightly decreased the viscosity values due to the distancing of collagen chains in the presence of cells<sup>22</sup>.

The crosslinking of the collagen was evaluated as a function of temperature (Fig. 1b). Initially, the storage modulus ( $G'$ ) was lower than the loss modulus ( $G''$ ), characteristic of a liquid-like material<sup>23</sup>. At  $31.6 \pm 0.6$  °C (crossover temperature), the storage modulus of the collagen became higher than the loss modulus, indicating a solid-like behavior. The presence of cells into the collagen matrix practically did not affect the crossover temperature ( $29.7 \pm 1.5$  °C). Therefore, we confirmed that the incubation temperature of 37 °C is adequate to crosslink the collagen structure.

Both storage and loss moduli were also measured as a function of angular frequency, after collagen reticulation (Fig. 1c). Both constructs (collagen with and without cells) displayed predominant elastic behavior ( $G' > G''$ ) throughout the angular frequency range, which is desirable for application in 3D bioprinting. Elasticity is the ability of a material to return to its original shape after deformation. Therefore, the elastic collagen bioink can aid in preserving the structural integrity of the printed construct<sup>24</sup>. The presence of cells into the collagen structure significantly improved both elastic and viscous behavior, which indicates that the fibroblasts contributed to the overall stiffness of the construct. Figure 1d displays the time sweep curves of collagen solutions with and without cells at 37 °C. From the start, both collagen solutions exhibited a solid-like structure, with the storage modulus surpassing the loss modulus. Notably, the curve profiles for both samples were highly similar. Within the initial 10 min at 37 °C, the most pronounced increase in the storage modulus occurred, indicating that the material becomes sufficiently tough to prevent drainage from the insert (Fig. 1d – inset). However, the storage modulus continued to slightly rise over the 60-minute duration, which represents the incubation time before epidermal incorporation during the fabrication of the human skin equivalent model. Although the collagen solutions with and without cells displayed similar rheological profiles, the  $G'$  values of the cell-laden gel were notably higher, attributed to the contribution of fibroblasts. This observation is consistent with findings from angular frequency sweep curves. This positive effect of cell presence on the mechanical property was confirmed by compression testing.

Stress-strain curves of reticulated collagen, dermis construct (collagen + fibroblast) and HSE show 4 stages of deformation: (i) elastic deformation, from which was extracted the elastic modulus; (ii and iii) different levels of plastic deformation of the collagen structure by alignment; and (iv) fractured construct (Fig. 1e). The elastic modulus increased from  $0.21 \pm 0.08$  kPa (collagen without cells) to  $41.8 \pm 0.4$  kPa for dermis construct and to  $52.1 \pm 1.8$  kPa for HSE. We observed that the presence of both fibroblasts and the epidermis positively affected the elastic modulus. This increase is a result of the interlocking network formed through cell-polymer and cell-cell interactions. The elastic modulus of the 3D skin model developed here is close to the human native skin (10–37 kPa)<sup>25,26</sup>. SEM micrographs show the fibrillar morphology of the collagen structure after crosslinking (Fig. 1f) and the high density of fibroblasts (Fig. 1g) attached to the collagen structure (dermis) of the 3D skin construct.

### Human skin equivalent with hypodermis morphological characterization

As already pointed out, new strategies for testing cosmetic or dermatological products have arisen worldwide to replace animal tests. Here, we focused on

advancing 3D skin models by incorporating the hypodermis layer. Our skin model comprises 3 layers: epidermis, dermis, and hypodermis (Fig. 1h–j). The hypodermis layer was constructed with a thick portion of collagen type I and adipocytes differentiated from hMSCs. Above this portion, the dermis equivalent was built up by bioprinting a mixture of dermal fibroblasts with collagen. Over the dermal portion, keratinocytes were deposited and differentiated, thus forming the epidermis (Fig. 2).

Skin equivalents serve as a highly valuable alternative to animal testing and can be considered physiologically comparable to natural skin<sup>27</sup>. Numerous companies have designed skin model alternatives to assess the efficacy of pharmaceutical, skincare, and cosmetic products in an in vitro platform, decreasing the dependency on animal usage. While HSE research has made significant progress in reconstructing dermal and epidermal layers using fibroblasts and keratinocytes, there is a requirement for innovative co-culture systems that can better emulate the intricacies of human anatomy<sup>28</sup>. Distinguished from other research cohorts that employed in vitro skin models by the incorporation of an explanted hypodermal layer<sup>13,28,29</sup>, our model was fabricated using the differentiated adipocyte cells from hMSC, using these cells our model has the advantages of reproducibility, high throughput, and control over internal structure, and shape compared to other techniques<sup>9–11</sup>.

To evaluate the structure of the HSEH, skin equivalents were harvested on day 10. Pictures of the 3D skin model showed the formation of the hypodermis layer on the basal portion. H&E staining (Fig. 2d) and SEM images also confirmed the presence of the hypodermis, with visible lipid droplets spaces in circular format and dense adipocyte population as shown under the dermis. The dermal portion of the skin model presented a homogenous distribution of the fibroblasts within the collagen structure and the epidermis comprised stratified layers of keratinocytes. In summary, the histological data confirmed the successful biofabrication of a robust skin model containing 3 differentiated layers, that closely mimic the native skin tissue structure. The achievement of a 3-layered model overcomes one notable challenge within the realm of bioengineering in vitro skin models<sup>6</sup>.

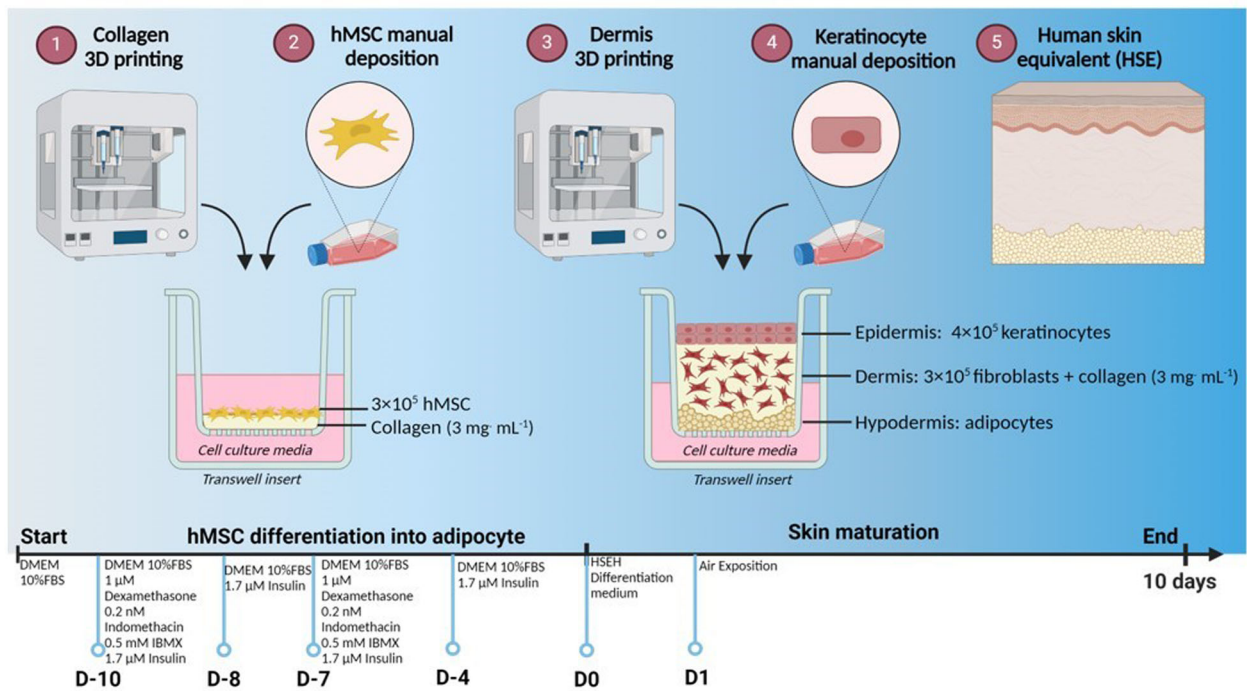
### HSEH physiology and gene signature

To characterize the physiology and transcriptome profile of the HSEH, we compared it to a two-layered HSE model. The difference between the two models is the presence of the hypodermis in the HSEH, which is absent in the HSE. Both models have identically constructed dermis and epidermis layers.

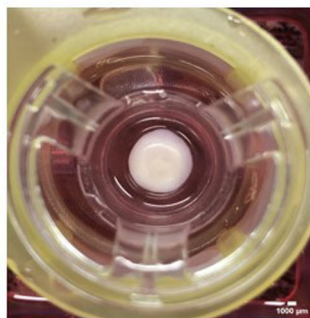
One of the principal challenges in the context of 3D cell culture pertains to the preservation of cell viability within the model<sup>30</sup>. To assess cell viability and proliferation in our models, we measured ATP production on both days 5 and 10 of skin differentiation, using it as an indirect indicator of cell viability (Fig. 3a). After luminescence measurement using the CellTiter-Glo® 3D cell viability assay, the ATP values were obtained using a standard curve (Supplementary Information, Fig. 1). The decrease in ATP values in 10 days of skin differentiation for both HSE and HSEH is likely attributed to the fact that, at this point, the differentiation process has stabilized, and the cells have entered a less metabolically active state.

To evaluate the integrity of the skin barrier, we performed TEER measurements, which is a reliable methodology to study barriers permeability and integrity. Here, we evaluated the HSEH in comparison with HSE at days 5 and 10 of skin differentiation. This method involves applying an alternating current (AC) across a membrane to gauge electrical resistance<sup>31</sup>. Through this approach, we can assess the condition of tight junctions and identify any indications of barrier dysfunction. The results of skin integrity through TEER revealed that HSEH exhibited significantly higher TEER values compared to HSE, demonstrating a 50% increase (Fig. 3b). This distinctive trend was consistently observed in measurements taken on both day 5 ( $p = 0.05$ ) and day 10 ( $p = 0.05$ ). The HSEH presented values around  $60 \Omega \cdot \text{cm}^2$ , corroborating with the values found in the human skin explants<sup>32</sup>. Compared to other complex full-thickness models, the HSEH presented superior values, indicating that it better mimics human skin<sup>33</sup>.

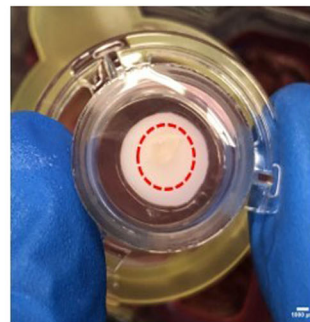
**a**



**b**



**c**



**d**

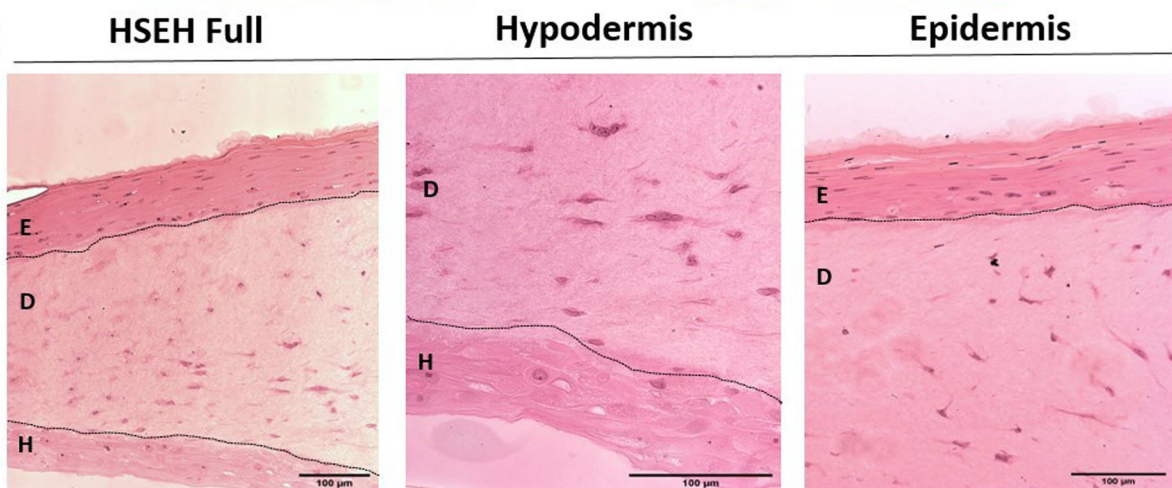
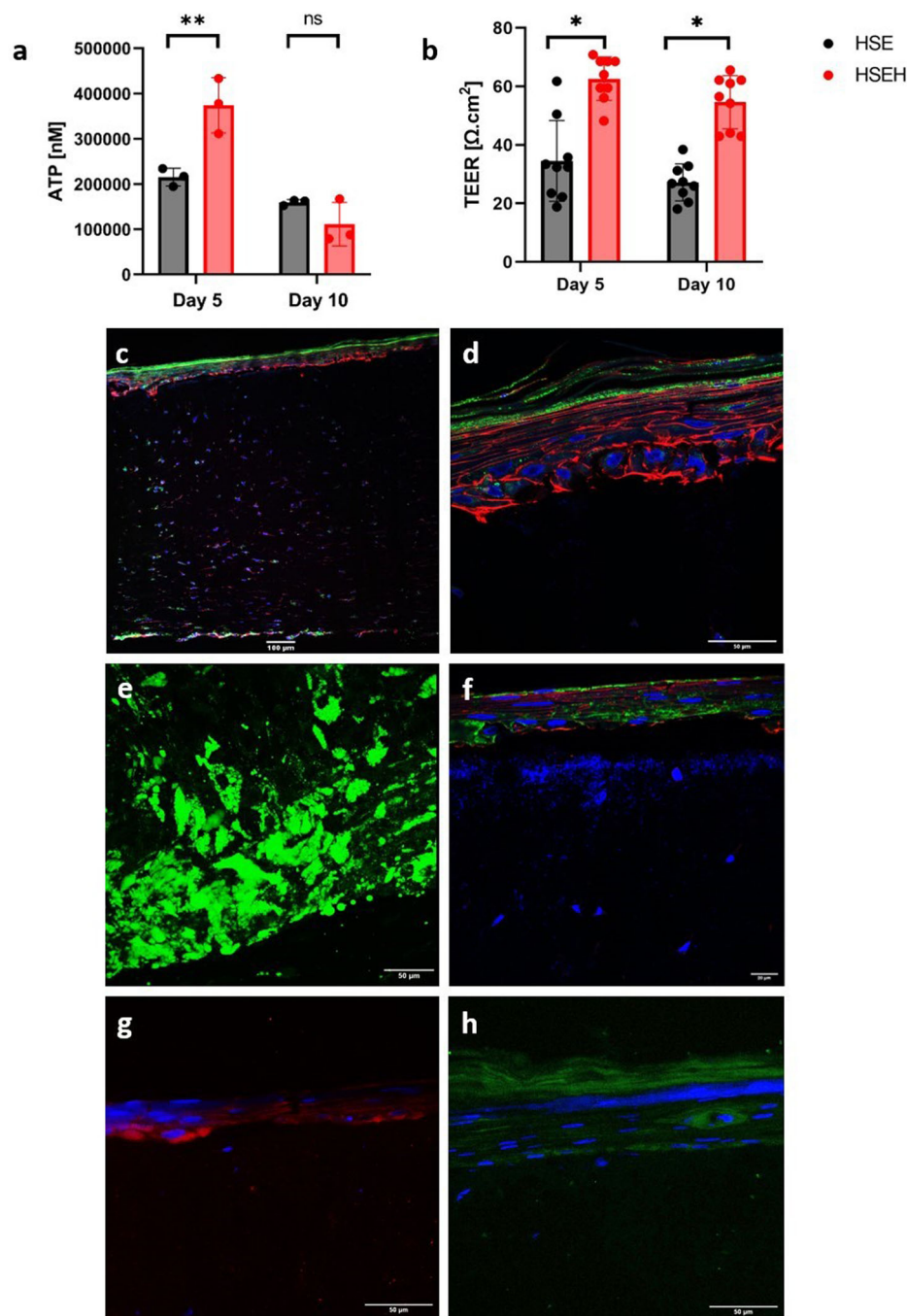


**Fig. 2 | Morphological characterization of the bioprinted human skin equivalent with hypodermis (HSEH).** **a** Scheme of production of HSEH model. Created in BioRender. Figueira, A. (2024) BioRender.com/x38z313. **b** Photo of apical view and (c) basal portion of the HSEH, highlighting the hypodermis layer. **d** Hematoxylin

and eosin-stained histological sections of HSEH model. The first image shows the full thickness image, the second shows the hypodermis region, and the third image the epidermis layer. The regions marked with E correspond to the epidermis, D to the dermis, and H to the hypodermis.

**Fig. 3 | HSEH cell viability, proliferation, and differentiation.** **a** ATP measurement comparison between HSE and HSEH at days 5 and 10. **b** Trans-epithelial electrical resistance (TEER) ( $\Omega \cdot \text{cm}^2$ ) measured at days 5 and 10. **c** Full image of HSEH differentiation after 10 days. **d** High magnification of hypodermis layer of HSEH showing the lipids droplets inside the adipocytes in green. **e** High magnification of epidermis of HSEH showing lipids labeled with bodipy in green, actin filaments labeled with phalloidin-rhodamine in red, and cell nuclei labeled with DAPI in blue. **f** HSEH epidermis labeling for involucrin (green), actin filaments (red), and cell nuclei (blue). **g** Immunolabeling of Cytokeratin 10 (red) in the epidermis of HSEH and **(h)** immunolabeling of Cytokeratin 15 (green). Graphic symbols denote significance levels:  $*P \leq 0.05$ . In the graph A dots represent  $n = 3$  biologically independent samples and in the graph (b), the dots represent  $n = 6$ .



The HSE (Supplementary Information, Fig. 2) and HSEH models were subjected to an immunostaining assay to evaluate the epidermis differentiation through protein expression, and bodipy staining to assess the adipocyte lipid content on hypodermis layer.

After keratinocytes stop proliferating, they migrate upwards to form the suprabasal layer, where they begin expressing differentiation markers like cytokeratins 1 and 10 (CK1/CK10)<sup>34</sup>. Cytokeratin 15 (CK15), typically expressed in basal keratinocytes, plays a role in maintaining the stem cell population before differentiation occurs. Eventually, the keratinocytes reach the outermost layer of the epidermis, where they form the cornified layer (stratum corneum) and express terminal differentiation markers such as loricrin and filaggrin<sup>34,35</sup>. In Fig. 3g, the expression of CK10 is evident as a marker of keratinocyte differentiation, while Fig. 3h shows the distribution of cytokeratin 15, highlighting keratinocytes that are on the path to

differentiation. The presence of cytokeratin corroborates with the data from the RNA sequencing (Supplementary Information, Fig. 3) showing the upregulation of cytokeratin 1, 4, 10, and 15 of HSEH compared to HSE.

Involucrin, the major protein component of the cornified cell envelope found in terminally differentiated epidermal cells<sup>36</sup>, was also monitored by immunostaining. The involucrin was consistently expressed in HSEH model, indicating its similarity with human skin tissue, and pointing out its feasibility as a good marker for evaluation of skin differentiation (Fig. 3f). In the same way, it was possible to observe that the hypodermis was well formed after the differentiation of hMSCs into adipocytes, which were successfully evidenced by bodipy identification (Fig. 3e). It was possible to observe lipids present in the dermis and epidermis as well.

The immunofluorescence images of the HSEH demonstrate remarkable similarities to actual human skin<sup>37-39</sup>. The outermost layer, the stratum

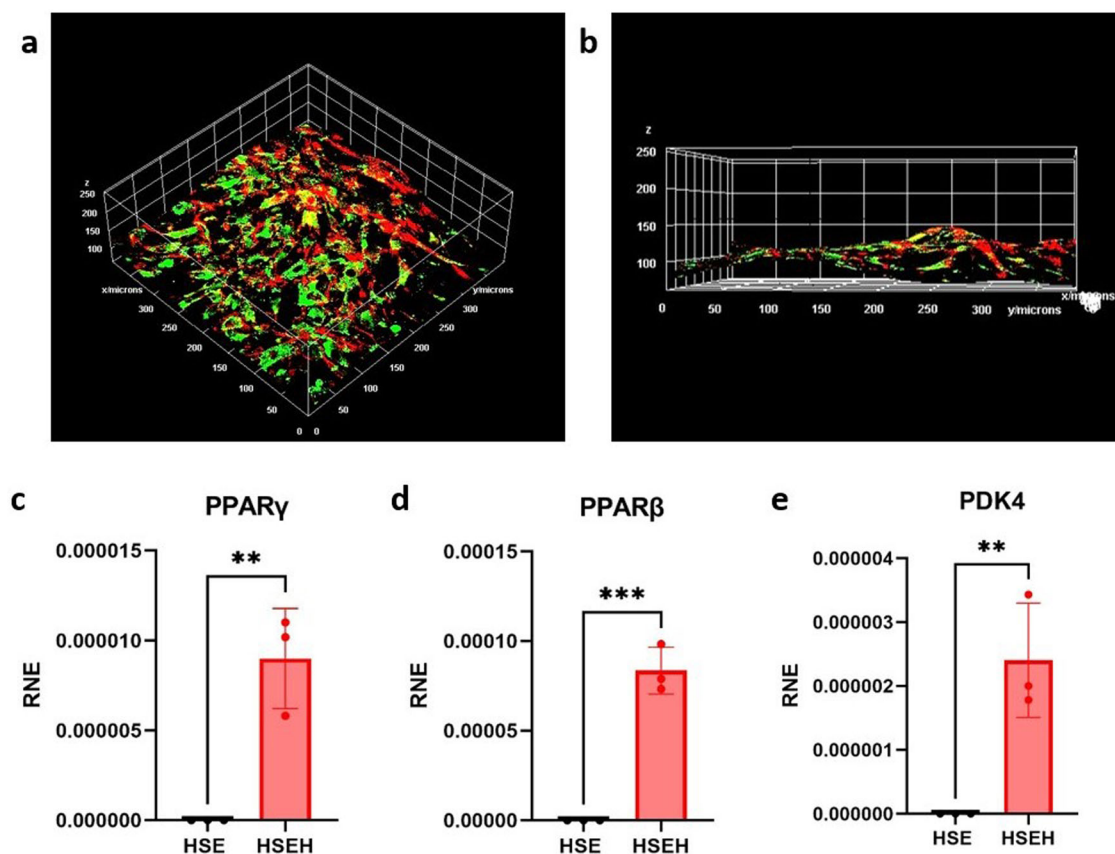


**Fig. 4 | Adipogenic differentiation of hMSCs and mRNA expression profile of genes regulated during the adipogenesis.** a, b 3D surface projections of a basal view of hypodermis. Cells were stained with phalloidin (red) to mark the actin in the cytoplasm, highlighting the boundaries of each cell, and with bodipy (green) to mark

the lipid droplets. Expression of (c) PPAR $\gamma$ , (d) PPAR $\beta$  and (e) PDK4 genes analyzed by qRT-PCR in the HSE and HSEH. Error bars represent standard deviation of means from at least 3 replicates ( $n = 3$ ). Graphic symbols denote significance levels: \* $P \leq 0.05$ , \*\* $P \leq 0.01$ , \*\*\* $P \leq 0.001$ .

corneum, appears as a thin, brightly stained band due to the presence of keratinized cells. The stratum spinosum shows a network of cells with intercellular bridges, stained for proteins like involucrin. The basal layer, adjacent to the dermis, contains more rounded cells with prominent nuclei. All these features can be observed in Fig. 3e that highlight the ultrastructure of HSEH epidermis. The dermis contains dispersed fibroblasts, elongated within the extracellular matrix (Fig. 3f). In the hypodermis, the most prominent feature is the presence of adipocytes. These cells are typically large, round, and have a characteristic ring-like appearance due to the large lipid droplet within them that displaces the nucleus to the periphery. Lipid-specific stains, such as Bodipy, highlight these droplets, usually resulting in bright green staining.

Besides staining lipid droplets with bodipy to assess the adipogenic differentiation of hMSCs within the 3D collagen type I hypodermal layer, we also evaluated the expression of adipocyte markers at the mRNA level (as shown in Fig. 4). The presence of PPAR $\gamma$ , PPAR $\beta$ , and PDK4 as specific markers for adipocytes, was assessed in reconstructed hypodermis after 10 days of culture using qPCR. hMSCs cultured in adipogenic conditions within the collagen hydrogels exhibited differentiation into adipocytes expressing the respective markers, while the control HSE did not show this expression (as depicted in Fig. 4c–e).

A comprehensive in vitro human skin model should aim to recapitulate the intricate structural composition of native skin, encompassing various cell types. Our model endeavors to mirror the fundamental architectural layers of the skin while emulating the physiological characteristics of these layers in an in vitro context. The hypodermal layer demonstrates the upregulation of distinctive markers associated with adipose tissue (PPAR $\gamma$ , PPAR $\beta$ , and PDK4), while faithfully reproducing the

organizational arrangement and lipid accumulation patterns for adipocytes. The PPAR $\gamma$  and the mTORC1 is related with upregulation of subcutaneous fat adiponectin secretion and the glyceroneogenesis in the hypodermis<sup>40</sup>. The expression PDK4 is closely associated with glyceroneogenesis<sup>41,42</sup>, while PPAR $\beta$  showed to stimulate differentiation and lipid accumulation in keratinocytes<sup>43</sup>. We also investigated other adipocyte-specific morphology through 3D whole-mount fluorescence staining of bodipy in differentiated hydrogels in vitro. The differentiated adipocytes were evenly distributed throughout the hydrogels and displayed numerous lipid droplets within their cytoplasm, as evidenced by the green color (bodipy) staining (illustrated in Fig. 3c) and observed across the entire hydrogel (as demonstrated in the Z-stack image in Fig. 4a, b).

To fully understand the gene expression signature of our HSEH model in comparison to the HSE model, we performed a transcriptomic evaluation through an RNA-sequencing analysis. The next-generation RNA sequencing (RNA-seq) provides unprecedented detail about the transcriptional landscape of our in vitro model, not only allowing for precise measurement of transcript expression levels in HSEH, but also showing how our model is assembling in vitro the genes pathways of the skin.

Gene ontology (GO) enrichment analysis was performed to determine pathways and functions associated with the identified Differentially Expressed Gene (DEGs). Comparative transcriptome analysis revealed distinct gene expression patterns, including pathways associated with adipogenesis, regulation of epidermal differentiation, and collagen synthesis and modulation. In detail, a gene was considered DEG when it exhibited a  $p \leq 0.005$ . According to this metric, out of the 28,163 analyzed genes, 1081 were identified as DEGs in the HESH compared to HSE, with 61.98% upregulated and 38.02% downregulated (Fig. 5b). The volcano plot

highlighted the upregulation of genes mainly associated to remodeling and organization of extracellular matrix and lipid metabolism (Fig. 5a). The most upregulated gene was Hyaluronan and Proteoglycan Link Protein 1 (HAPLN1), a protein involved in crosslinking and stabilizing hyaluronic acid (HA) with aggregates of proteoglycan monomers. The function of HAPLN1 is believed to influence collagen and ECM contraction. A study was conducted to understand the role of HAPLN1 in skin, finding that its expression decreases with age. This decrease is associated with alterations in the extracellular matrix (ECM) and consequent impairment of vascular integrity, which, in turn, influences metastasis and inflammatory cell infiltration<sup>44,45</sup>. Given that HAPLN1 is essential for a normally functioning ECM, the up regulation of this gene in the HSEH model suggests that the presence of hypodermis enhances ECM structure and functionality.

The functional analysis highlighted 12 significant biological processes (BP) when we compared HSEH with HSE (Fig. 5c). In the enrichment of gene clusters, dots represent term enrichment with color coding: red indicating high enrichment, while gray indicating low enrichment. The sizes of the dots represent the percentage of each row (GO category), the graph confirming the influence of the hypodermis in ECM modulation. Upregulated genes showed enrichment in terms related to ECM processes, with the most significant being ‘collagen-containing extracellular matrix,’ ‘external encapsulating structure,’ and ‘extracellular matrix’ (Fig. 5c, d). These results demonstrate the robustness of our 3-layered model, as literature highlights the crucial interaction between the hypodermis and dermis in maintaining skin homeostasis, as recently reviewed<sup>46</sup>. Furthermore, we can assume that the presence of a functional hypodermis ensures a robust dermal ECM, influencing key dermal properties such as strength and elasticity<sup>46</sup>.

From the GO-enriched terms, we highlighted the molecular function ‘collagen binding’ (Fig. 6a) and the cellular component ‘collagen trimer’ (Fig. 6b), both crucial to the composition and reliability of the skin ECM. Collagen trimerization and interactions with binding proteins are essential for the integrity and functionality of the skin ECM. The triple helix of the three collagen molecules provides structural strength and stability, while binding proteins like proteoglycans and glycoproteins enhance the framework and assist in the organization and crosslinking of ECM fibers. Together, these processes ensure the resilience, elasticity, and functionality of the skin<sup>47</sup>.

Additionally, an enrichment in the biological process term ‘regulation of keratinocyte differentiation’ was observed (Fig. 6c), confirming that the presence of the hypodermis influences not only the dermis but also the outermost layer of the skin, the epidermis. The expression of structural proteins such as cytokeratin 10 (KRT10) is used as a marker for skin maturation and the establishment of an effective barrier<sup>48</sup>. In this study, KRT10 was one of the upregulated genes in HSEH, further suggesting that HSEH is more effective in structuring the skin barrier.

As expected, the addition of hypodermis to the skin model promoted the expression of genes related to lipid metabolism, as evidenced by the GO enrichment on the canonical pathways of leptin and adiponectin (Fig. 6d). The expression of these genes creates a more physiologically relevant environment, enhancing the model’s robustness and making it more suitable for studying a variety of skin disorders. Adipokines like leptin and adiponectin act as hormones and cytokines, playing crucial roles in skin homeostasis. They are involved in structural functions such as angiogenesis and collagen production and provide the skin with anti-inflammatory tools to combat pathogens, thereby maintaining its structural and functional integrity<sup>49,50</sup>.

Our model showed that the subcutaneous layer, or hypodermis, played a key role in the epidermal differentiation, ECM proteins expression, and skin hydration, which are related to the regulation of the adipocytes layer. Some reports have identified that the presence of hypodermis caused a positive regulation in the differentiation of in vitro skin models through the increased number of actively dividing basal cells, the deposition of basement membrane proteins, and the increase of cells transformed into fully mature

keratinocytes, ultimately optimizing the formation of a multi-layered epithelial structure<sup>13,51</sup>.

The transcriptome data presented here highlights crucial pathways that are enriched in the HSEH, demonstrating their significant involvement in skin function. This achievement opens an opportunity to apply the HSEH model in a wide range of assays, compromising it to the ‘3Rs’ principle. This principle encompasses Replacement, Reduction, and Refinement in humane animal research<sup>13</sup>, and it is globally recognized and firmly embedded in numerous national and international regulations.

This groundbreaking research has revealed the development of a 3D skin model remarkably resembling native human skin, composed of epidermis, dermis and hypodermis. Using 3D bioprinting, we achieved automation to fabricate the HSEH constructs with great cell organization. The collagen hydrogel has provided structural, mechanical, and biological cues to skin cells functions. This model faithfully replicated the architectural layers of native skin and exhibited upregulation of specific markers associated with adipose tissue, skin differentiation, and skin hydration. The HSEH’s transcriptome profile unveiled essential biological processes, such as epidermis development, ECM remodeling, and lipid metabolism. Additionally, the model’s enriched pathways highlighted its potential for various research applications, aligning with the ‘3Rs’ principle and regulatory measures aimed at reducing animal experimentation. Overall, the HSEH model represents a promising and ethically sound tool for advancing the field of dermatological research.

## Methods

### Cell culture before biofabrication of constructs

Human mesenchymal stem cells (hMSC, PT-2501, Lonza) were cultured in MSCBM Basal Media (Lonza) and MSCGM SingleQuots Supplement Kit (Lonza) and were used up to passage 6. Human dermal fibroblasts cells provided from BCRJ were extracted from foreskin of a black male with 2 years old (HDFn, nh-skp-FB0040, Banco de Células do Rio de Janeiro, Brazil), cultured in Dulbecco’s modified Eagle medium (DMEM 12-604, Lonza) with 4.5 g L<sup>-1</sup> glucose and L-glutamine supplemented with 10% (w/v) fetal bovine serum (FBS, VitroCell), and they were used up to passage 20. Primary human keratinocytes provided from BCRJ were extracted from foreskin of a black male with 7 years old (HEKn, nh-skp-KT0009, Banco de Células do Rio de Janeiro, Brazil), cultured in EpiLife™ medium (MEPI500CA, Gibco) with 60 μM Ca<sup>+2</sup> supplemented with human keratinocyte growth supplement (HKGS S-001-5, Gibco), and they were used up to passage 5. All cell culture were performed in an incubator (Thermo) at 37 °C, humidified, 5% CO<sub>2</sub> environment.

### Collagen preparation previous to biofabrication of constructs

For each well, 525 μL of collagen I from rat tail (Corning; concentration of 3 mg mL<sup>-1</sup>) was mixed with 70 μL of HAM F-12 (Gibco; 10x), 70 μL of reconstitution buffer (10x), and 35 μL of FBS. The reconstitution buffer was prepared by mixing 50 μM NaOH, 261 mM NaHCO<sub>3</sub> and 200 mM HEPES (All from Sigma Aldrich). After mixing, the solution was transferred to a volumetric flask and completed to 50 mL. After preparation, the reconstitution buffer was sterilized with 0.2 μm filter, aliquoted and kept at -20 °C until use. During collagen preparation, the solution was kept on ice to prevent reticulation.

### Human skin equivalent (HSE) and human skin equivalent with hypodermis (HSEH) fabrication

**Hypodermis fabrication.** A thin layer of collagen (200 μL) was printed on a transwell insert (Corning; 12 mm Transwell® with 0.4 μm pore polyester membrane insert) using a commercial bioprinter (Genesis, 3D Biotechnology Solutions, Brazil). The plate was incubated for 1 h at 37 °C for collagen crosslinking. After this time, 3 × 10<sup>5</sup> of hMSC (in 500 μL of DMEM with 10% FBS) were manually deposited on top of the collagen (Fig. 2a). The plate was incubated at 37 °C in an incubator with 5% CO<sub>2</sub> during 11 days for cell differentiation into adipocytes. Initially, DMEM

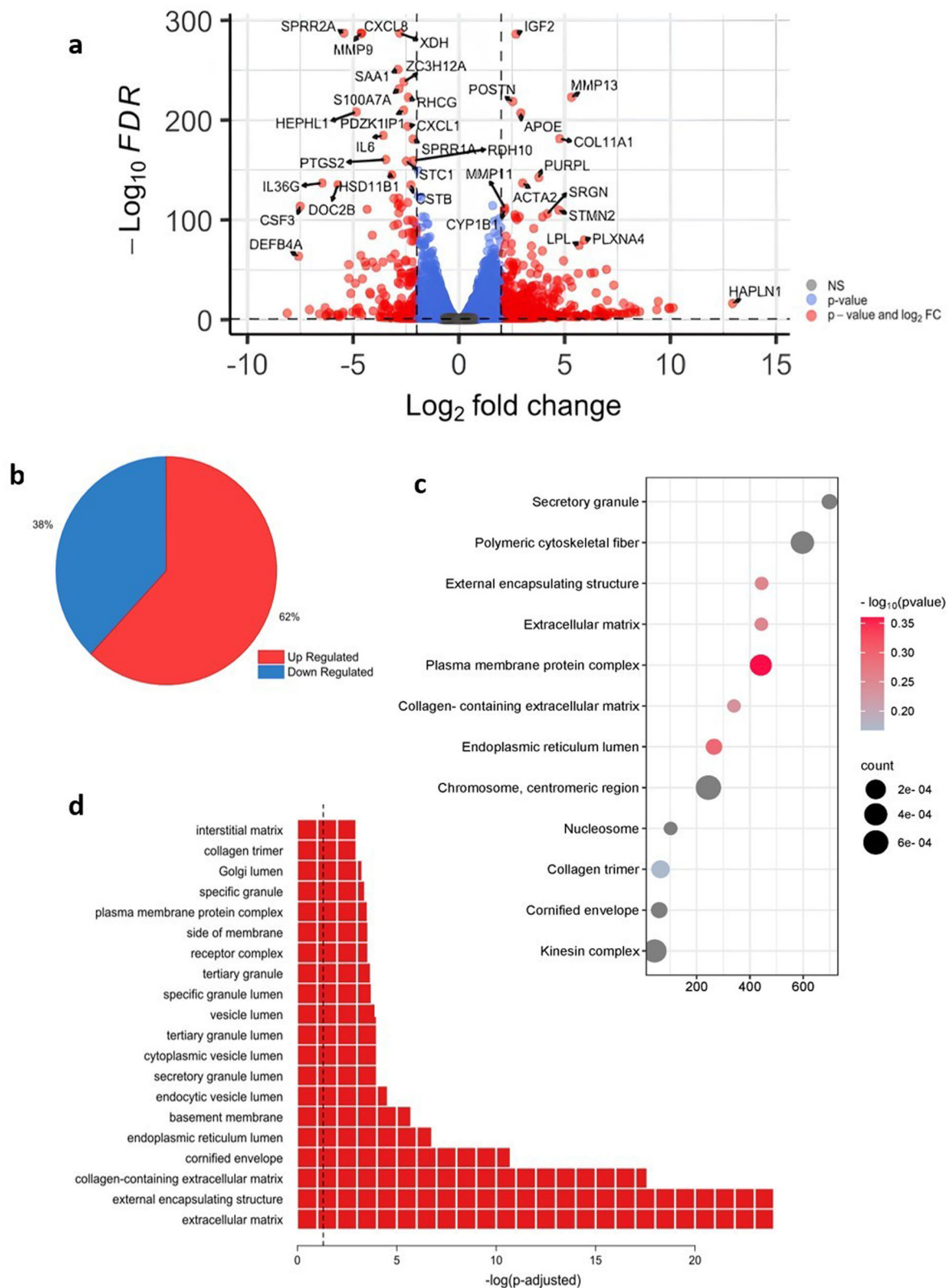


**Fig. 5 | Identification of DEGs comparing HSEH to HSE.** **a** Volcano plot shows data for the transcriptome. Threshold in axis Y indicates 1.5 and in axis X indicates  $\text{log}_2$  fold change. Blue dots represent genes out of the threshold, red dots are the up and down regulated genes and gray dots are non-significant genes. **b** Part-to-whole

chart indicate the percentage of up- and down-regulated genes among the identified DEGs (Total: 1081 genes). **c** Biological process analysis plot of the 12 most enriched process when comparing HSEH with HSE. **d** The graph expresses the 20 most GO enriched process in the HSEH.  $N = 3$  biologically independent samples.



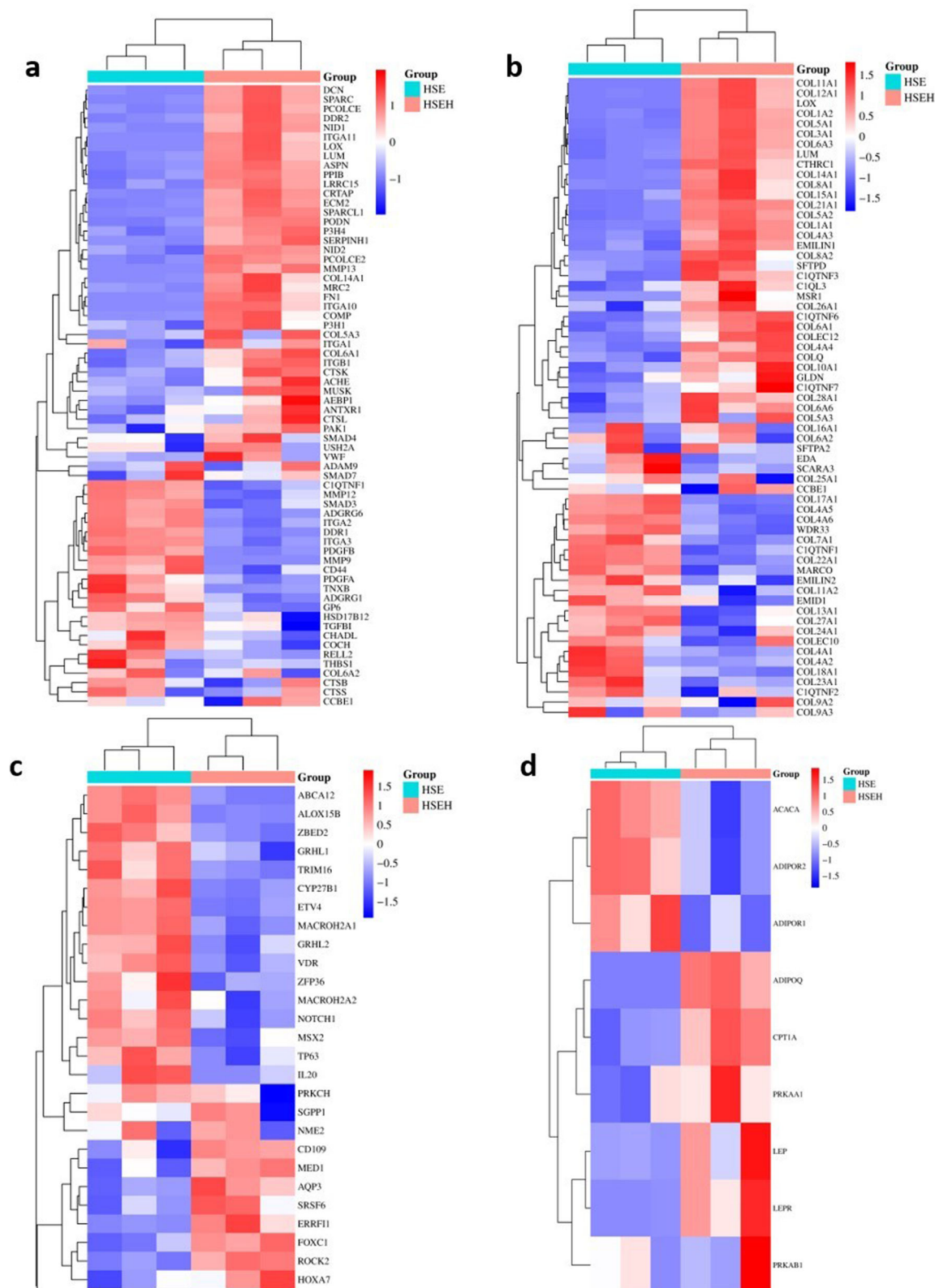


**Fig. 6 | Heat map of the enrichment analysis. a** Collagen binding. **b** Collagen trimmer. **c** Keratinocyte differentiation. **d** Leptin and Adiponectin. Target genes are colored by increasing statistical significance (turquoise to red). *N* = 3 biologically independent samples.

with 10% FBS (Basal medium) was used as cell culture media (D-11, Fig. 2a). After 1 day of cultivation (D-10), the culture medium was changed for a differentiation medium that consist into Basal medium supplemented with 1  $\mu$ M of dexamethasone, 0.2 nM of indomethacin, 0.5 mM of IBMX and 1.7  $\mu$ M of insulin (all from Sigma-Aldrich). In the

3rd day of cultivation (D-8, Fig. 2a), the DMEM with 10% FBS was supplemented only with 1.7  $\mu$ M of insulin and, in the next day (D-7, Fig. 2a), the differentiation medium was used for cell adipocyte differentiation. Finally, between 7 and 11 days of cultivation (D-4 to D0, Fig. 2a) DMEM with 10% FBS with 1.7  $\mu$ M of insulin was used. The

culture medium was placed inside (500  $\mu\text{L}$ ) and outside (1000  $\mu\text{L}$ ) the insert.

**Dermis fabrication.** After 11 days of hypodermis biofabrication and differentiation, and at the initial day of HSE fabrication (D0, Fig. 2a), 700  $\mu\text{L}$  of collagen solution containing  $3 \times 10^5$  of fibroblasts were 3D bioprinted on top of the insert with or without the hypodermis layer. The construct was designed in the Thinker Cad software and consisted of 9 layers of concentric circles. The Simplify 3D software (Simplify 3D, V5) was used for slicing and to control the bioprinter. The bioink was placed in a 10 mL sterile syringe (Luer-Lock, BD) coupled to an irrigation needle with a nozzle diameter of 0.7 mm (22 G, Injex). The temperature of the syringe holder was set to 4  $^{\circ}\text{C}$  and the construct was printed with speed of 60  $\text{mm s}^{-1}$ . After the printing process, the plate was incubated for 1 h at 37  $^{\circ}\text{C}$  for collagen crosslinking.

**Epidermis fabrication.** Right after the dermis crosslinking, for both HSEH and HSE,  $4 \times 10^5$  of keratinocytes were manually deposited on top of the insert using 200  $\mu\text{L}$  of cell culture media, composed of 100  $\mu\text{L}$  of EpiLife™ and 100  $\mu\text{L}$  of a differentiation medium prepared by mixing: 100 mL of DMEM-F12, 100  $\mu\text{L}$  of 10  $\text{mg.mL}^{-1}$  insulin (Sigma, I2643) in 5  $\mu\text{M}$  HCl (Sigma Aldrich) 400  $\mu\text{L}$  of 1  $\mu\text{M}$  hydrocortisone 21-hemisuccinate sodium salt (Sigma, H4881) in ethanol (Sigma Aldrich) and DMEM (1:1), 25  $\mu\text{L}$  of 2  $\mu\text{g.mL}^{-1}$  epidermal growth factor (Sigma, E9644) in DMEM, 100  $\mu\text{L}$  of 5  $\text{mg.mL}^{-1}$  apo-transferrin (Sigma, T1147) in water, and 10  $\mu\text{L}$  of 1  $\mu\text{M}$  cholera toxin (Sigma, C8052) in sterile purified water. Since this layer did not demand ECM components, the cells were manually added and not printed. The constructs were incubated for 24 h, and the medium in the apical portion of the insert was aspirated to form an air liquid interface, and the inserts were moved to a deep well plate (Falcon 355467) with a cell strainer (Falcon 352360). The differentiation medium supplemented as described above was kept only outside of the insert (9 mL) for the following 10 days, changing the media every 3 days.

### Evaluation of the viscous properties by rheology

The rheological properties of the collagen were evaluated with and without fibroblasts using a compact modular rheometer (MCR-102, Anton Paar, Austria), controlled by the Anton Paar Rheoplus software (RHEOPLUS/32 version 3.61). A cone-plate geometry with 50 mm of diameter was positioned with 0.097 mm between the plates. Viscosity measurements were performed as a function of shear rate (1.0 to 300  $\text{s}^{-1}$ ) at 25  $^{\circ}\text{C}$ , immediately after gel preparation (without crosslinking), to simulate 3D bioprinting conditions. The storage ( $G'$ ) and loss ( $G''$ ) moduli were measured as a function of temperature, immediately after gel preparation, to evaluate temperature-driven crosslinking. For temperature sweep, a constant angular frequency of 10  $\text{rad. s}^{-1}$ , coupled with 1% of strain was applied, using a heating rate of 2  $^{\circ}\text{C.min}^{-1}$  and temperature ranging from 10 to 70  $^{\circ}\text{C}$ . Furthermore,  $G'$  and  $G''$  were measured as a function of oscillation frequency (0.1 and 17  $\text{rad. s}^{-1}$ ) using crosslinked collagen after 10 days of cell culture. For these measurements, a plate-plate geometry with 10 mm diameter and 1.0 mm gap was used. For the oscillation frequency measurement, a constant strain of 1% was applied, which lies within the linear viscoelasticity area. For time sweep, the collagen solutions with and without fibroblasts were analyzed immediately after gel preparation (without crosslinking), using temperature of 37  $^{\circ}\text{C}$ , 1% strain, and angular frequency of 10  $\text{rad. s}^{-1}$ . All measurements were performed in triplicate. The graphs were plotted using GraphPad Prism, version 9.5.1.

### Mechanical characterization by compression testing

The mechanical properties of the constructs were evaluated in a texture analyzer (TA.XTplus, Stable Micro Systems, UK) using a 500 N load cell. The equipment was controlled by the Exponent TA.XTplus software, version 6.2. The collagen constructs without cells were measured immediately after crosslinking (1 h at 37  $^{\circ}\text{C}$ ). In addition, the skin model containing

dermis (collagen with fibroblasts), and epidermis (keratinocytes) was measured after 10 days of cell culture. A construct containing only the dermis layer (collagen with fibroblasts) was also fabricated and measured after 10 days of cell culture. The cylindrical constructs were compressed up to 100% strain with a probe diameter of 75 mm and compression rate of 0.05  $\text{mm. s}^{-1}$ . The elastic modulus was extracted from the initial linear region of the stress-strain curves, using the OriginPro 2023 software. All measurements were performed in triplicate.

### Morphology assessment by scanning electron microscopy (SEM)

The morphology of the crosslinked collagen without cells and the cell laden 3D skin construct were analyzed by field emission gun-SEM (FEG-SEM Inspect F50, Thermo Fisher Scientific, USA). Secondary electron (SE) images were acquired with acceleration voltage of 3 kV. Sample preparation for SEM included: (i) washing with phosphate buffered saline (DPBS) (Gibco); (ii) overnight fixation of the constructs at 4  $^{\circ}\text{C}$  in a solution containing 2.5% of glutaraldehyde and 0.1 M of sodium cacodylate buffer with 1.5 mM of  $\text{CaCl}_2$  (all from Sigma Aldrich); (iii) dehydration in gradient ethanol solutions (30%, 50%, 70%, 90% and 100%), 10 min each; (iv) drying at 25  $^{\circ}\text{C}$ ; (v) cutting with blade for cross-sectional view; and (vi) deposition of a thin layer of gold. The ImageJ software, version 1.54d, was used to add the scale bar to all images, following calibration with a reference-scaled image.

### Barrier integrity analysis by trans-epithelial electrical resistance (TEER)

The barrier integrity of HSE and HSEH models was evaluated by TEER. Measurements were taken using an Epithelial Volt/Ohm Meter (Millicell® ERS-2 Voltohmmeter) and a pair of Ag/AgCl probes (Milipore). TEER values were calculated according to Eq. 1:

$$\text{TEER} = (R_{\text{sample}} - R_{\text{blank}}) \times A \quad (1)$$

where  $R_{\text{sample}}$  is the resistance value for the skin model,  $R_{\text{blank}}$  is the resistance value of an insert without cultured cells, and  $A$  the effective culture area (1.12  $\text{cm}^2$ ). Briefly, the differentiation medium was removed, 2 mL of PBS were added in the basal region, and additional 300  $\mu\text{L}$  of PBS were added in the apical region for the measurements. The probe was placed such that one electrode was submerged in the upper compartment and the other was submerged in the lower compartment. TEER values were recorded on day 5 and day 10 of skin differentiation. These measurements were performed in 3 batches of 3 reconstituted skin models at each time. The graph was plotted using GraphPad Prism, version 9.5.1.

### Cell viability by the ATP measurement

To evaluate the proliferation state of HSE and HSEH cultures, after day 5 and day 10 of skin differentiation, the models were harvested from the inserts and placed in a white 96-well plate with 100  $\mu\text{L}$  of culture medium. The ATP of each tested condition was quantified using a CellTiter-Glo® 3D Cell Viability Assay (Promega) following the manufacturer's instructions. The luminescence was recorded in a Glow Max Plate Reader (Promega, USA). The graphs were plotted using GraphPad Prism, version 9.5.1.

### Cell differentiation by immunofluorescence

HSE and HSEH models were fixed at day 5 and day 10, for 4 h in 10% formalin (Sigma Aldrich) and embedded in a cryopreservative medium (OCT, Tissue Tek, Sakura) and immediately frozen at  $-20^{\circ}\text{C}$ , after which the blocks were sectionized in 10  $\mu\text{m}$  sections using a cryostat (Leica). The sections were fixed on a glass slide for 10 min at ambient temperature. To perform the immunolabeling, the sections were washed three times with PBS, incubated with permeation solution (0.1% Triton X-100), for 15 min at room temperature, washed 3 times with PBS, and blocked for 2 h, with 2% bovine serum albumin (BSA, Sigma-Aldrich). After blocking, samples were incubated with primary antibody anti-involucrin (Thermo MA5-11803),

anti-cytokeratin 10 (Thermo MA5-13705), and anti-cytokeratin 15 (Abcam AB52816) overnight, at 4 °C, in a humidify chamber. Subsequently to incubation with primary antibody, samples were washed 3 times with PBS and incubated for 2 h with secondary antibody anti-mouse (Thermo A110001 and A11032) and anti-rabbit (Thermo A11034). Nuclei were stained with DAPI (Biotium) for 5 min, actin fibers with phalloidin rhodamine (Thermo) and lipids droplets with Bodipy (Cayman) for 40 min before image acquisition. Images were acquired in a confocal laser scanning microscope (TCS SP8, Leica) using the software LAS X 5.0.2. The ImageJ software, version 1.54d, was used to add the scale bar to all images, following calibration with a reference-scaled image.

### Structure by histology trough historesin embedding and hematoxylin and eosin staining

The samples were fixed in 10% buffered formalin from the dilution of 37% formaldehyde solution (Sigma-Aldrich) in PBS at pH 7.4. Subsequently, they were gradually dehydrated in ethanol (30, 50, 70, 80, 90, 95, and 100%) and embedded in historesin (Leica). Previous to embedding, the ethanol of the samples was gradually replaced by the historesin (ethanol:historesin ratio of 5:1, 4:1, 3:1, 2:1, 1:1, and 1:2). A rotating microtome (RM2235, Leica) was used to cut the samples, with the aid of glass slides made from glass strips for ultramicrotome (Ted Pella, USA) in a Glass Knife Maker (EM KMR3, Leica). Transverse cuts were made with thickness of 5 µm and transferred to 76 × 26 mm microscopy slides (Waldemar Knittel). For hematoxylin & eosin (H&E) staining, the historesin sections were incubated at 40 °C in Harris hematoxylin (Scientific ACS), for 15 min, and rinsed in running water for 3 min. Subsequently, sections were incubated at 40 °C, for 15 min in an aqueous solution of 0.5% eosin Y (Sigma-Aldrich) and 0.5% Phloxine B (Sigma-Aldrich) and rinsed under running water for 3 min. After drying, the slides were assembled with Entellan® new (Sigma-Aldrich) and 24 × 50 mm covers (Exacta) for further analysis in an optical microscope (DM6, Leica). The ImageJ software, version 1.54d, was used to add the scale bar to all images, following calibration with a reference-scaled image.

### Transcriptome Illumina library preparation and sequencing

To prepare the transcriptome libraries, approximately 150 ng of total RNA from each sample was processed using the Illumina Stranded Total RNA Prep, Ligation Kit with Ribo-Zero Plus (Illumina Inc., San Diego, CA, USA), following the manufacturer's instructions. Library quality was validated with the D5000 ScreenTape Assay Kit for the TapeStation 4150 (Agilent) and quantified using qPCR with the QIAseq Library Quant Assay Kit (Qiagen). The libraries were pooled in equimolar ratios (650 pM) and submitted for paired-end sequencing (2 × 100 bp) on the Illumina NextSeq 2000 platform at the Brazilian Biorenewables National Laboratory (LNBR/CNPEM) in Campinas, Brazil.

FastQC<sup>52</sup> was employed to assess the quality of the sequencing reads. Skewer<sup>53</sup> was then utilized to trim low-quality ends using the parameters (--mode pe --end-quality 20 --mean-quality 20 --min 30), as recommended by previously published guidelines<sup>54</sup>. The trimmed reads were aligned to the GRCh38 genome using STAR<sup>55</sup>. Subsequently, transcript abundance was quantified with HTSeq<sup>56</sup>. Differential expression analysis was conducted with DESeq2<sup>57</sup>, following the removal of unwanted variation via RUVSeq<sup>58</sup>. Pathway enrichment analysis was carried out using clusterProfiler<sup>59</sup> and ReactomePA<sup>60,61</sup>. Signature scoring was performed with singscore<sup>62</sup>, using reference sets from REACTOME<sup>61</sup>, MSigDB<sup>63</sup> or WikiPathways<sup>64</sup>. The raw reads were deposited in the Sequence Read Archive (SRA) under the access code PRJNA1139958.

### Statistics and Reproducibility

The data were analyzed in GraphPad Prism software, version 9.5.1, using t-student test nonparametric. Statistical significance was established at a p value of less than 0.05. All data points were derived from two or more biological replicates. Replicates were defined through manufacturing of skin constructs on different days, utilizing cells from distinct passage numbers,

and employing varied collagen lots to ensure comprehensive and diverse data representation.

### Reporting summary

Further information on research design is available in the Nature Portfolio Reporting Summary linked to this article.

### Data availability

The data that support the findings of this study that are available in the supplementary Data 1 and the raw reads from RNAseq were deposited in the Sequence Read Archive (SRA) under the access codes PRJNA1139958.

Received: 11 December 2023; Accepted: 21 October 2024;

Published online: 11 November 2024

### References

- Sarkiri M, Fox SC, Fratila-Apachitei LE, Zadpoor AA. Bioengineered Skin Intended for Skin Disease Modeling. *Int J Mol Sci.* **20**, 1475 (2019)
- Zhang M, Zhang C, Li Z, Fu X, Huang S. Advances in 3D skin bioprinting for wound healing and disease modeling. *Regen Biomater.* **10**, rbac105 (2022)
- Vilela de Sousa I, Ferreira MJS, Bebiano LB, Simões S, Matos AF, Pereira RF, Granja PL. Skin models of cutaneous toxicity, transdermal transport and wound repair. *Burns Trauma.* **11**, tkad014 (2023).
- Footner, E. et al. Layer-by-Layer Analysis of *In Vitro* Skin Models. *ACS Biomater Sci. Eng.* <https://doi.org/10.1021/acsbomaterials.3c00283> (2023).
- Workman, V. L., Giblin, A.-V., Green, N. H., MacNeil, S. & Hearnden, V. Development of a tissue-engineered skin model with epidermal, dermal and hypodermal components. *In vitro Models* <https://doi.org/10.1007/s44164-023-00058-9> (2023).
- Hofmann E, Schwarz A, Fink J, Kamolz LP, Kotzbeck P. Modelling the Complexity of Human Skin *In Vitro.* *Biomedicines.* **11**, 794 (2023).
- Roger, M. et al. Bioengineering the microanatomy of human skin. *J. Anat.* **234**, 438–455 (2019).
- Jorgensen, A. M. et al. Multicellular bioprinted skin facilitates human-like skin architecture in vivo. *Sci. Transl. Med.* **15**, eadf7547 (2023).
- Kang MS, Jang J, Jo HJ, Kim WH, Kim B, Chun HJ, Lim D, Han DW. Advances and Innovations of 3D Bioprinting Skin. *Biomolecules.* **13**, 55 (2022).
- He P, Zhao J, Zhang J, Li B, Gou Z, Gou M, Li X. Bioprinting of skin constructs for wound healing. *Burns Trauma.* **6**, 5 (2018).
- Li, J. et al. Engineering functional skin constructs: a quantitative comparison of three-dimensional bioprinting with traditional methods. *Exp. Dermatol.* **31**, 516–527 (2022).
- Chambers ES, Vukmanovic-Stejic M. Skin barrier immunity and ageing. *Immunology.* **160**, 116–125 (2020).
- Zimoch, J. et al. Bio-engineering a prevascularized human tri-layered skin substitute containing a hypodermis. *Acta Biomater.* **134**, 215–227 (2021).
- Bambace, C. et al. Inflammatory profile in subcutaneous and epicardial adipose tissue in men with and without diabetes. *Heart Vessels* **29**, 42–48 (2014).
- Veronese S, Picelli A, Smania N, Sbarbati A. Hypodermis involvement in skin disorders: Imaging and functional imaging diagnostic tools. *Skin Res Technol.* **27**, 641–643 (2021).
- Schmidt, F. F., Nowakowski, S. & Kluger, P. J. Improvement of a three-layered in vitro skin model for topical application of irritating substances. *Front. Bioeng. Biotechnol.* **8**, 388 (2020).
- Kim, B. S. et al. Engineering of diseased human skin equivalent using 3D cell printing for representing pathophysiological hallmarks of type 2 diabetes in vitro. *Biomaterials* **272**, 120776 (2021).
- Gudapati, H., Parisi, D., Colby, R. H. & Ozbolat, I. T. Rheological investigation of collagen, fibrinogen, and thrombin solutions for drop-on-demand 3D bioprinting. *Soft Matter* **16**, 10506–10517 (2020).

19. Markstedt, K. et al. 3D bioprinting human chondrocytes with nanocellulose–alginate bioink for cartilage tissue engineering applications. *Biomacromolecules* **16**, 1489–1496 (2015).
20. van Kampen, K. A. et al. Biofabrication: from additive manufacturing to bioprinting. in *Reference Module in Biomedical Sciences* (Elsevier, 2019). <https://doi.org/10.1016/B978-0-12-801238-3.11118-3>.
21. Yang, H., Duan, L., Li, Q., Tian, Z. & Li, G. Experimental and modeling investigation on the rheological behavior of collagen solution as a function of acetic acid concentration. *J. Mech. Behav. Biomed. Mater.* **77**, 125–134 (2018).
22. Majumder, N., Mishra, A. & Ghosh, S. Effect of varying cell densities on the rheological properties of the bioink. *Bioprinting* **28**, e00241 (2022).
23. Mehrotra, S. et al. Nonmulberry Silk based ink for fabricating mechanically robust cardiac patches and endothelialized myocardium-on-a-chip application. *Adv. Funct. Mater.* **30**, 1907436 (2020).
24. Donderwinkel, I., van Hest, J. C. M. & Cameron, N. R. Bio-inks for 3D bioprinting: recent advances and future prospects. *Polym. Chem.* **8**, 4451–4471 (2017).
25. Yang, Y. et al. Quantitative assessment of skin stiffness using ultrasound shear wave elastography in systemic sclerosis. *Ultrasound Med. Biol.* **45**, 902–912 (2019).
26. Pailler-Mattei, C., Bec, S. & Zahouani, H. In vivo measurements of the elastic mechanical properties of human skin by indentation tests. *Med Eng. Phys.* **30**, 599–606 (2008).
27. Mertsching, H., Weimer, M., Kersen, S. & Brunner, H. Human skin equivalent as an alternative to animal testing. *GMS Krankenhhyg Interdiszip.* **3**, Doc11 (2008).
28. Sanchez, M. M., Tonmoy, T. I., Park, B. H. & Morgan, J. T. Development of a vascularized human skin equivalent with hypodermis for photoaging studies. *Biomolecules* **12**, 1828 (2022).
29. Huber, B. et al. Integration of mature adipocytes to build-up a functional three-layered full-skin equivalent. *Tissue Eng. Part C. Methods* **22**, 756–764 (2016).
30. Bikmulina, P. et al. 3D or not 3D: a guide to assess cell viability in 3D cell systems. *Soft Matter* **18**, 2222–2233 (2022).
31. Srinivasan B, Kolli AR, Esch MB, et al. TEER measurement techniques for in vitro barrier model systems. *Journal of Laboratory Automation.* **20**, 107–26 (2015).
32. Neil, J. E., Brown, M. B. & Williams, A. C. Human skin explant model for the investigation of topical therapeutics. *Sci. Rep.* **10**, 21192 (2020).
33. Zoio, P., Ventura, S., Leite, M. & Oliva, A. Pigmented full-thickness human skin model based on a fibroblast-derived matrix for long-term studies. *Tissue Eng. Part C. Methods* **27**, 433–443 (2021).
34. Zhou, Q. et al. Phenformin promotes Keratinocyte differentiation via the Calcineurin/NFAT Pathway. *J. Investig. Dermatol.* **141**, 152–163 (2021).
35. Fuchs, E. Epithelial skin biology: three decades of developmental biology, a hundred questions answered and a thousand new ones to address. *Curr. Top. Dev. Biol.* **116**, 357–374 (2016).
36. Murphy, G. F., Flynn, T. C., Rice, R. H. & Pinkus, G. S. Involucrin expression in normal and neoplastic human skin: a marker for keratinocyte differentiation. *J. Investig. Dermatol.* **82**, 453–457 (1984).
37. Caporali, S. et al. Post zygotic, somatic, deletion in KERATIN 1 V1 domain generates structural alteration of the K1/K10 dimer, producing a monolateral palmar epidermolytic nevus. *Int. J. Mol. Sci.* **22**, 6901 (2021).
38. Sun, K. L., Liu, W., Gao, X. M., Yang, M. & Chang, J. M. A study of normal epidermal melanocyte distribution. *Int. J. Dermatol. Venereol.* **4**, 32–35 (2021).
39. Zou, Z. et al. A single-cell transcriptomic atlas of human skin aging. *Dev. Cell* **56**, 383–397.e8 (2021).
40. Andrade, M. L. et al. PPAR $\gamma$ -induced upregulation of subcutaneous fat adiponectin secretion, glyceroneogenesis and BCAA oxidation requires mTORC1 activity. *Biochim. Biophys. Acta Mol. Cell Biol. Lipids* **1866**, 158967 (2021).
41. Cadoudal, T. et al. Pyruvate dehydrogenase kinase 4. *Diabetes* **57**, (2008).
42. Cadoudal, T. et al. Pyruvate dehydrogenase kinase regulation by thiazolidinediones and implication in glyceroneogenesis in adipose tissue. *Diabetes* **57**, 2272–2279 (2008).
43. Schmuth, M. et al. Peroxisome proliferator-activated receptor (PPAR)- $\beta/\delta$  stimulates differentiation and lipid accumulation in keratinocytes. *J. Investig. Dermatol.* **122**, 971–978 (2004).
44. Marino-Bravante, G. E. et al. Age-dependent loss of HAPLN1 erodes vascular integrity via indirect upregulation of endothelial ICAM1 in melanoma. *Nat. Aging* **4**, 350–363 (2024).
45. Kaur, A. et al. Remodeling of the collagen matrix in aging skin promotes melanoma metastasis and affects immune cell motility. *Cancer Discov.* **9**, 64–81 (2019).
46. Liu, M., Lu, F. & Feng, J. Aging and homeostasis of the hypodermis in the age-related deterioration of skin function. *Cell Death Dis.* **15**, 443 (2024).
47. Huang, J. et al. Dermal extracellular matrix molecules in skin development, homeostasis, wound regeneration and diseases. *Semin. Cell Dev. Biol.* 128 Preprint at <https://doi.org/10.1016/j.semcdb.2022.02.027> (2022).
48. Bhar, B., Das, E., Manikumar, K. & Mandal, B. B. 3D bioprinted human skin model recapitulating native-like tissue maturation and immunocompetence as an advanced platform for skin sensitization assessment. *Adv. Health. Mater.* **13**, e2303312 (2024).
49. Dopytalska K, Baranowska-Bik A, Roszkiewicz M, Bik W, Walecka I. The role of leptin in selected skin diseases. *Lipids Health Dis.* **19**, 215 (2020).
50. Oh, J. et al. The role of adiponectin in the skin. *Biomol. Ther.* **30**, 221–231 (2022).
51. Monfort, A., Soriano-Navarro, M., García-Verdugo, J. M. & Izeta, A. Production of human tissue-engineered skin trilayer on a plasma-based hypodermis. *J. Tissue Eng. Regen. Med.* **7**, 479–490 (2013).
52. Leggett RM, Ramirez-Gonzalez RH, Clavijo BJ, Waite D, Davey RP. Sequencing quality assessment tools to enable data-driven informatics for high throughput genomics. *Front Genet.* **4**, 288 (2013).
53. Jiang H, Lei R, Ding SW, Zhu S. Skewer: a fast and accurate adapter trimmer for next-generation sequencing paired-end reads. *BMC Bioinformatics.* **15**, 182 (2014).
54. Del Fabbro C, Scalabrin S, Morgante M, Giorgi FM. An extensive evaluation of read trimming effects on Illumina NGS data analysis. *PLoS One.* **8**, e85024 (2013).
55. Dobin A, Davis CA, Schlesinger F, Drenkow J, Zaleski C, Jha S, Batut P, Chaisson M, Gingeras TR. STAR: ultrafast universal RNA-seq aligner. *Bioinformatics.* **29**, 15–21 (2013).
56. Anders S, Pyl PT, Huber W. HTSeq—a Python framework to work with high-throughput sequencing data. *Bioinformatics.* **31**, 166–9 (2015).
57. Love MI, Huber W, Anders S. Moderated estimation of fold change and dispersion for RNA-seq data with DESeq2. *Genome Biol.* **15**, 550 (2014).
58. Risso, D., Ngai, J., Speed, T. P. & Dudoit, S. Normalization of RNA-seq data using factor analysis of control genes or samples. *Nat. Biotechnol.* **32**, 896–902 (2014).
59. Wu, T. et al. clusterProfiler 4.0: a universal enrichment tool for interpreting omics data. *Innovation* **2**, 100141 (2021).
60. Yu, G. & He, Q. Y. ReactomePA: an R/Bioconductor package for reactome pathway analysis and visualization. *Mol. Biosyst.* **12**, 477–479 (2016).
61. Milacic, M. et al. The Reactome Pathway Knowledgebase 2024. *Nucleic Acids Res.* **52**, D672–D67 (2024).
62. Bhuva, D. D., Cursons, J. & Davis, M. J. Stable gene expression for normalisation and single-sample scoring. *Nucleic Acids Res.* **48**, e113 (2020).

63. Liberzon, A. et al. The molecular signatures database hallmark gene set collection. *Cell Syst.* **1**, 417–425 (2015).
64. Agrawal, A. et al. WikiPathways 2024: next generation pathway database. *Nucleic Acids Res.* **52**, D679–D689 (2024).

## Acknowledgements

This research used facilities of the Brazilian Nanotechnology National Laboratory (LNNano), the Brazilian Biorenewables National Laboratory (LNBR), the Brazilian Synchrotron Light Laboratory (LNLS), and the Brazilian Biosciences National Laboratory (LNBio), part of the Brazilian Centre for Research in Energy and Materials (CNPEM), a private non-profit organization under the supervision of the Brazilian Ministry for Science, Technology, and Innovations (MCTI). The Tissue Engineering Laboratory (LEnT), the Laboratory of Bioimaging (LIB) [proposal 20220501], the Spectroscopy and Calorimetry Laboratory (LEC) [proposal 20233053], the Electron Microscopy Laboratory facility [proposal numbers 20230035 and 20233352], the Next Generation Sequencing (NGS) facility [proposal 202440872] staff is acknowledged for the assistance during the experiments. This work was supported by the “Fundação de Amparo à Pesquisa do Estado de São Paulo” (FAPESP) [2022/14725-6], CNPq “Conselho Nacional de Desenvolvimento Científico e Tecnológico” [303948/2022-1] and CNPEM.

## Author contributions

T.M.A., A.C.M.F., and S.V.H. devised the experimental plan for this study, and T.M.A., S.V.H., R.A.A., F.A.H.B., L.C.M.O., and R.J.A. carried out the experimental work. D.A. performed the RNAseq data analysis. C.D.S.H., A.C.M.F., P.G., and M.A.A. devised the structure of the manuscript, and T.M.A., S.V.H., and C.D.S.H. drafted and wrote the manuscript. T.M.A. and S.V.H. created figures used unless otherwise stated. A.C.M.F., M.D., V.K.T., P.G., and M.A.A. revised the manuscript critically and suggested references. A.C.M.F. supervised the project and acquired funding for the project. All authors have read and approved the final submitted manuscript.

## Competing interests

The authors declare no competing interests.

## Additional information

**Supplementary information** The online version contains supplementary material available at <https://doi.org/10.1038/s42003-024-07106-4>.

**Correspondence** and requests for materials should be addressed to Ana Carolina M. Figueira.

**Peer review information** *Communications Biology* thanks the anonymous reviewers for their contribution to the peer review of this work. Primary Handling Editor: Ophelia Bu.

**Reprints and permissions information** is available at <http://www.nature.com/reprints>

**Publisher's note** Springer Nature remains neutral with regard to jurisdictional claims in published maps and institutional affiliations.

**Open Access** This article is licensed under a Creative Commons Attribution-NonCommercial-NoDerivatives 4.0 International License, which permits any non-commercial use, sharing, distribution and reproduction in any medium or format, as long as you give appropriate credit to the original author(s) and the source, provide a link to the Creative Commons licence, and indicate if you modified the licensed material. You do not have permission under this licence to share adapted material derived from this article or parts of it. The images or other third party material in this article are included in the article's Creative Commons licence, unless indicated otherwise in a credit line to the material. If material is not included in the article's Creative Commons licence and your intended use is not permitted by statutory regulation or exceeds the permitted use, you will need to obtain permission directly from the copyright holder. To view a copy of this licence, visit <http://creativecommons.org/licenses/by-nc-nd/4.0/>.

© The Author(s) 2024